



Design and Optimization of Open-cladded Plasmonic Waveguides for CMOS Integration on Si₃N₄ Platform

E. Chatzianagnostou¹ · D. Ketzaki¹ · G. Dabos¹ · D. Tsiokos¹ · J.-C. Weeber² · A. Miliou¹

Received: 14 June 2018 / Accepted: 28 September 2018 / Published online: 6 October 2018
© Springer Science+Business Media, LLC, part of Springer Nature 2018

Abstract

Herein, we present a design analysis and optimization of open-cladded plasmonic waveguides on a Si₃N₄ photonic waveguide platform targeting CMOS-compatible manufacturing. For this purpose, two design approaches have been followed aiming to efficiently transfer light from the hosting photonic platform to the plasmonic waveguide and vice versa: (i) an in-plane, end-fire coupling configuration based on a thin-film plasmonic structure and (ii) an out-of-plane directional coupling scheme based on a hybrid slot waveguide. A comprehensive numerical study has been conducted, initially deploying gold as the reference metal material for validating the numerical models with already published experimental results, and then aluminum and copper have been investigated for CMOS manufacturing revealing similar performance. To further enhance coupling efficiency from the photonic to the plasmonic part, implementation of plasmonic tapering schemes was examined. After thorough investigation, plasmophotonic structures with coupling losses per single interface in the order of 1 dB or even in the sub-dB level are proposed, which additionally exhibit increased tolerance to deviations of critical geometrical parameters and enable CMOS-compatible manufacturing.

Keywords CMOS metals · Photonic integrated circuits · Plasmonics · Silicon nitride · Surface waves

Introduction

Plasmonic waveguides have attracted significant research interest due to their unique features and unmatched advantages. By supporting surface electromagnetic waves known as surface plasmon polaritons (SPPs), plasmonic waveguides can confine and guide light below the diffraction limit at sub-wavelength scales [1, 2] reducing the size of optical components down to that of nano-electronic transistors. However, inherent high propagation losses of plasmonic waveguides stemming from their metallic nature, in conjunction with the broad adoption of noble metals like gold (Au) and silver (Ag) hamper their broad deployment in photonic integrated circuits (PICs). To overcome those limitations and fully exploit the profound benefits of plasmonic technology, two technology

directives have to be followed: (1) selectively co-integrate nano-scale plasmonics with low-loss photonic components and (2) replace noble metals with alternative CMOS-compatible counterparts enabling volume manufacturing of high-performance plasmophotonic ICs.

Some remarkable efforts to co-integrate specific plasmonic and photonic waveguides in hybrid structures and functional modules were recently reported [3–23]. While the vast majority of these structures exploit silicon (Si) as the photonic waveguide platform [3–15], silicon nitride (Si₃N₄) has been also deployed [16–22], as a cheaper technology alternative offering wider wavelength transparency from visible to infrared as well as photonic waveguides with lower propagation losses and relaxed fabrication tolerances [24, 25]. Moreover, silicon nitride is a commonly used material in CMOS electronic fabrication processes (etch masking, passivation, strain engineering), therefore enabling CMOS-compatible integrated photonics [26]. Regarding the plasmonic structure, the two dominant waveguide types in literature are based on metal stripes [12–20] and metallic slot configurations [3–11, 21, 22]. A key challenge when integrating those types of plasmonic waveguides with photonics in order to minimize overall chip losses is to maximize the power coupling from the photonic to the plasmonic part. Regarding stripe-based plasmonic

✉ E. Chatzianagnostou
evachat@csd.auth.gr

¹ Department of Informatics, Center for Interdisciplinary Research and Innovation, Aristotle University of Thessaloniki, 57001 Thessaloniki, Greece

² Laboratoire Interdisciplinaire Carnot de Bourgogne, UMR 6303 CNRS-Université de Bourgogne, 21078 Dijon, France

waveguides, the required photonic-to-plasmonic waveguide transition has been accomplished so far by either end-fire [12–17] or directional coupling schemes [18–20]. In the metallic slot configurations, the power transfer is achieved by exploiting the directional coupling mechanism [3–5, 22] or by means of mode conversion from the photonic to the plasmonic mode [6–11, 21]. However, in most cases DLSPP waveguides [12–15] or embedded in dielectric material plasmonic structures are reported [3–5, 8, 11, 18, 19] leaving biosensing applications far behind their performance limits due to the partial exploitation of the electromagnetic field at the metal interface. On the contrary, uncladded versions of SPP waveguides may be leveraged as very efficient transducers in integrated sensors due to the extraordinary exposure of the optical field at the metal-analyte interface [10, 20]. In addition, adoption of noble metals has been the dominant tendency regarding the plasmonic material. Although individual studies relying on CMOS-compatible metals like aluminum (Al) and copper (Cu) have reported promising results [3, 6, 17, 21, 27–31], a systematic approach to study and evaluate the capabilities of such materials and structures on Si₃N₄-based photonic waveguides is missing.

Towards this direction, in this paper, we present a systematic methodology to efficiently co-integrate those two fundamental types of plasmonic waveguides on a Si₃N₄ photonic waveguide platform towards (i) low-loss plasmo-photonic structures and (ii) CMOS compatibility. In parallel, we focus on open-cladded, liquid-loaded structures that may be subsequently adopted as optical transducer elements in integrated biosensors, although applications like ultra-short interconnects, optical switches or electro-optic modulators [7, 9, 13, 15, 17] are also possible. In this framework, two different routes were followed for the design of the interface between the photonic and the plasmonic waveguides. In the first case, an end-fire, in-plane coupling approach was used to couple light from a Si₃N₄ bus waveguide to a thin-film plasmonic waveguide with finite width [32]. The second approach concerns a hybrid plasmo-photonic waveguide configuration which exploits off-plane directional coupling to vertically transfer light from a Si₃N₄ ridge waveguide to a metal slot waveguide. Before proceeding to the CMOS-based design analysis, we present a thorough numerical investigation of both thin-film and slot configurations using gold as the reference metal in order to extract a general design route for each coupling scheme applicable to different materials and platforms and to allow for validation with already reported experimental relevant results [16, 22]. Coupling efficiency in the proposed configurations has been optimized beyond the reported values in [16, 22] by the implementation of plasmonic tapering schemes leading to coupling loss even in the sub-dB region. Relying on those outcomes, we extended our investigation to account for CMOS compatibility by replacing gold with the low-cost materials of aluminum and copper in the

plasmonic waveguides paving the way towards volume manufacturing of plasmo-photonic integrated circuits. Data from experimental characterization have been used for the refractive index of all the investigated metals (Au, Al, Cu) [31]. Furthermore, the fabrication tolerance of the proposed structures with respect to key geometrical parameters has been examined demonstrating high tolerance to possible structural deviations.

The rest of this paper is organized as follows: firstly, the detailed design analysis including fabrication tolerances of both end-fire and directional coupling schemes is presented for the case where gold is utilized as the plasmonic metal material. This analysis provides the functional characteristics for both thin-film and slot configurations that are subsequently used for the design of the CMOS-compatible configurations. In the next section, plasmonic tapering methods are investigated to further enhance coupling efficiency. Following the optimization section, extension of the Au-based designs by replacing gold with the CMOS fab compatible materials aluminum and copper as the plasmonic metal is described. A comparative overview is presented in the next section, while in the last section, a brief summary and concluding remarks are provided.

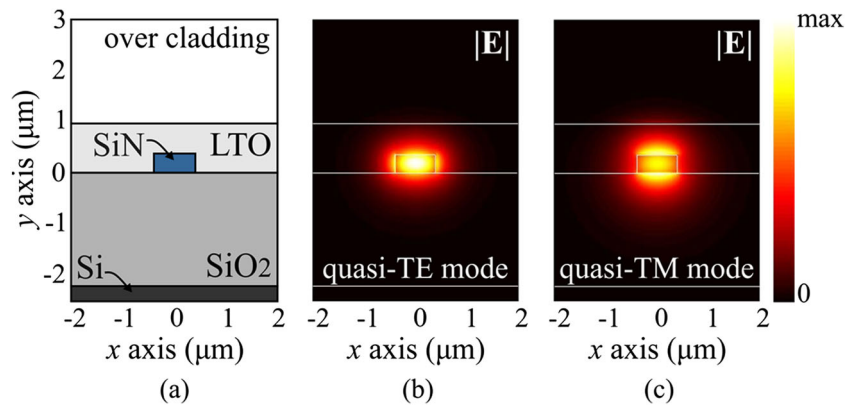
Design of Gold-Based Structures

The Si₃N₄-based waveguide platform selected in this work is based on a 360 nm × 800 nm Si₃N₄ ridge waveguide ($n_{\text{Si}_3\text{N}_4} = 1.996$ [33]) located on top of a 2.2 μm thick buried oxide (SiO₂) substrate ($n_{\text{SiO}_2} = 1.444$ [34]) and cladded by a 600 nm low-temperature oxide (LTO), ($n_{\text{LTO}} \equiv n_{\text{SiO}_2}$). Such a Si₃N₄ waveguide layer can be developed in a CMOS fab either at the front-end of line (FEOL) process using low-pressure chemical vapor deposition (LPCVD) or at the back-end of line (BEOL) using plasma-enhanced chemical vapor deposition (PECVD) at the cost of additional losses at 1550 nm [26].

To identify the supported photonic modes for this configuration and detect their modal characteristics, a thorough eigenvalue analysis was conducted using a commercial-grade finite-difference-based eigenmode solver [35]. It was found that this waveguide can support two fundamental photonic modes at the wavelength of interest, i.e., 1550 nm: the quasi-TE and the quasi-TM. These modes are then used for the excitation of the surface plasmon polariton in the directional coupling (slot waveguide) and end-fire (thin-film waveguide) scheme, respectively.

The cross-sectional geometry of the Si₃N₄ waveguide along with the electric field distributions of the two fundamental supported modes are depicted in Fig. 1. For this waveguide and air as the over cladding, the effective indices obtained with 2D eigenvalue analysis are $n_{\text{eff}}^{(\text{TE})} = 1.577$ and

Fig. 1 **a** 2D cross-sectional geometry of the Si₃N₄-based photonic waveguide. **b, c** Electric field distributions for the quasi-TE and quasi-TM photonic modes, respectively



$n_{\text{eff}}^{(\text{TM})} = 1.517$ for the quasi-TE and the quasi-TM photonic mode, respectively.

End-Fire Thin-Film Structure

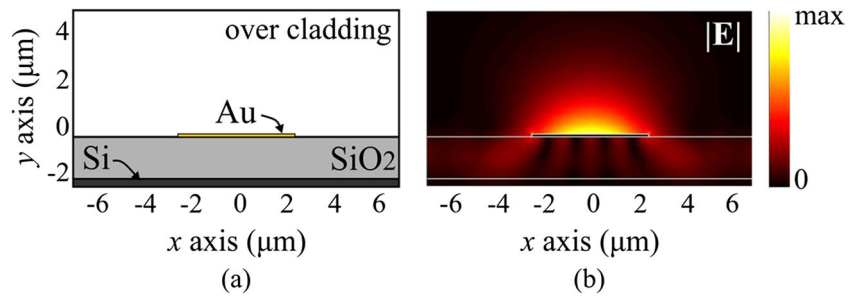
In what follows, we present the detailed design analysis of the first coupling scenario that relies on an end-fire configuration adopting gold as the plasmonic metal. It consists of the Si₃N₄ photonic waveguide and an Au-based thin film with finite width plasmonic waveguide. The metallic stripe ($n_{\text{Au}} = 0.26 - 11.0009i$ [31]) resides on a SiO₂ substrate and has a thickness of 100 nm. Additionally, it is open-cladded (without any dielectric on top) so that it can be potentially exposed to any surrounding medium. In our design approach, a water layer ($n_{\text{water}} = 1.311 - 0.0001348i$ [34]) has been adopted as the overlying medium (over cladding) so as to optimally mimic the aqueous environments potentially found in biosensing applications. The 2D cross-sectional geometry of the whole structure can be seen in Fig. 2a.

This plasmonic thin-film configuration has been numerically analyzed by the same eigenmode solver to detect its supported modes and specify their modal characteristics. It was found that this structure is capable of supporting a fundamental TM plasmonic mode mostly concentrated above the metal layer and exhibiting a maximum on the metal-cladding interface. Although the modal properties of the plasmonic mode are strongly dependent on the refractive index of the overlying material, the geometry of the Au stripe and especially its width (w_{Au}) is also a crucial parameter that affects the modal characteristics of this plasmonic waveguide. More specifically, when w_{Au} is decreased the plasmonic mode’s propagation losses are increasing till the cutoff width of approximately 4.5 μm, below which the plasmonic mode cannot be supported. Figure 2b shows the plasmonic mode of interest for $w_{\text{Au}} = 5 \mu\text{m}$ (slightly above the cutoff width). The effective index derived from this eigenmode study was $n_{\text{eff}} = 1.315 - 0.002631i$ leading to a propagation length (L_{SPP}) equal to 48 μm, that is the e-folding distance of the optical intensity.

In order to efficiently transfer the light between the photonic Si₃N₄ waveguide and the thin-film plasmonic structure, spatial mode matching between the photonic and the plasmonic mode should be achieved. The polarization of the plasmonic mode field components dictates that coupling is possible only to the fundamental quasi-TM mode of the Si₃N₄ waveguide. Therefore, the spatial distributions of the quasi-TM photonic and the TM plasmonic mode should be spatially matched. More specifically, given the field distributions of these two modes for the initial geometry setup, the extent of the photonic mode at the x -axis (Fig. 1c) is quite smaller compared with that of the plasmonic mode (Fig. 2b). Additionally, the two modes are not center-aligned along the y -axis. Consequently, the Si₃N₄ mode cannot fully contribute to coupling, since its lower part is hidden by the metallic stripe. In order to improve spatial matching, both widening the Si₃N₄ mode with respect to the horizontal (x) direction, as well as centering the two modes along the vertical (y) direction is necessary. The Si₃N₄ mode widening can be achieved either by reducing the Si₃N₄ ridge width, as this tends to relax mode confinement, or by broadening the physical width of the Si₃N₄ core which will naturally expand the photonic mode horizontally. In this work, we chose the second route considering that narrowing the Si₃N₄ would increase the propagation losses while cumbering fabrication requirements. Moreover, eigenmode analysis revealed that the photonic mode exhibits marginal n_{eff} changes in the order of 0.001 for $\Delta w_{\text{SiN}} = 1 \mu\text{m}$ when w_{SiN} increases above the cutoff width of the plasmonic waveguide ($w_{\text{SiN}} > 4.5 \mu\text{m}$). With respect to the center alignment along the y direction, it can be accomplished by introducing a vertical offset (h_{offset}) between the two waveguides along this direction. Following this rationale, in what follows, critical geometrical dimensions of the interface will be varied, in pursuit of maximum coupling efficiency.

Towards this objective, a detailed power overlap integral analysis between the two modes has been performed. This analysis aims to provide a qualitative indication of the appropriate cross-sectional geometry along with the necessary vertical offset so that optimum performance is achieved. The

Fig. 2 **a** 2D cross-sectional geometry of the thin-film plasmonic waveguide. **b** Electric field distribution for the TM plasmonic mode



vector overlap integral (OI) calculation has been performed by using the following equation

$$OI = \frac{\left| \iint \mathbf{E}_{ph} \times \mathbf{H}_{pl}^* \cdot \hat{z} dS \right|^2}{\left| \iint \mathbf{E}_{ph} \times \mathbf{H}_{ph}^* \cdot \hat{z} dS \right| \cdot \left| \iint \mathbf{E}_{pl} \times \mathbf{H}_{pl}^* \cdot \hat{z} dS \right|}, \quad (1)$$

where \mathbf{E} , \mathbf{H} describe the vector of electric and magnetic field distributions, whereas the distinction between photonic and plasmonic mode is denoted with subscripts (\mathbf{E}_{ph} , \mathbf{H}_{ph} for the photonic and \mathbf{E}_{pl} , \mathbf{H}_{pl} for the plasmonic). Equation (1) is evaluated on the cross-sections (S) of the two waveguides under study.

Equation (1) is expected to provide the fraction of the guided power that can be transferred from the photonic to the plasmonic mode and/or backwards. The overlap integral analysis was conducted varying the Au-stripe vertical position (along y direction) with reference to the basic Si_3N_4 waveguide (Fig. 3a, denoted as h_{offset} in Fig. 3b). That was repeated for several combinations of the Si_3N_4 waveguide and Au-stripe widths ($w_{\text{SiN}}/w_{\text{Au}}$) as presented in Fig. 3c.

For each width combination, a local maximum is observed for the overlap integral with respect to h_{offset} . This maximum tends to take larger values as both waveguide widths increase. Simultaneously, the mode matching is optimum when w_{SiN} is adjusted to a value almost equal to w_{Au} . The final selection of the appropriate cross-sectional dimensions though has been a compromise between the maximum spatial matching efficiency, low plasmonic propagation losses and the whole end-fire structure compactness.

As such, the optimal geometrical characteristics for the Au stripe and the Si_3N_4 photonic waveguide have been chosen so that the metal film is wide enough to achieve an overlap integral value above 50% and reasonable plasmonic propagation losses (0.05 dB/ μm) in compact dimensions. Thus, the exact cross-sectional dimensions for the Au stripe and the Si_3N_4 waveguide core were chosen $100 \text{ nm} \times 7 \text{ }\mu\text{m}$ and $360 \text{ nm} \times 7.5 \text{ }\mu\text{m}$, respectively, yielding a spatial matching capability (overlap integral value) almost 52% for a vertical offset distance, h_{offset} , 400 nm. Figure 4 depicts the mode profiles for the two selected waveguide cross-sections. The effective indices obtained at 1550 nm are $n_{\text{eff}}^{\text{ph}} = 1.608$ for the photonic and $n_{\text{eff}}^{\text{pl}} = 1.317 - 0.00143i$ for the thin-film plasmonic mode

with the latter exhibiting 0.05 dB/ μm propagation losses and a propagation length, L_{SPP} , of 86 μm . To guarantee that only the fundamental mode of the selected Si_3N_4 waveguide will be excited, a linear taper can be used between the basic Si_3N_4 waveguide ($360 \text{ nm} \times 800 \text{ nm}$) and the finally selected cross-section ($360 \text{ nm} \times 7.5 \text{ }\mu\text{m}$) to achieve adiabatic transfer between the two quasi-TM photonic modes (Fig. 1c and Fig. 4a) [16].

Going a step further, the aforementioned waveguide structures have been combined in an end-fire interface configuration as the one shown in Fig. 5a. The 3D model of this structure represents a single transition from the photonic to the plasmonic waveguide and has been numerically simulated by means of a commercial-grade simulator based on the finite-difference time-domain (FDTD) method [36] in order to verify the extracted results from the 2D overlap integral analysis and calculate the light coupling efficiency of the proposed structure. The opposite direction of propagation (from the plasmonic to the photonic waveguide) has been also examined leading to similar results. A side-view geometry of the proposed interface can be found in Fig. 5b illustrating the main parameters under investigation. As can be seen, apart from the vertical offset, h_{offset} , which was previously described, an additional parameter (L_{offset}) has been introduced representing a longitudinal offset at the photonic-to-plasmonic interface providing also the fabrication tolerance of the structure in metal deposition inaccuracies. Moreover, water has been utilized as the surrounding medium of the structure.

Figure 5c depicts the coupling loss of the proposed thin-film-based coupling scheme calculated for two different cases. Firstly, varying the h_{offset} between 0 and 1 μm for a fixed $L_{\text{offset}} = 0 \text{ }\mu\text{m}$ (blue curve) and then varying the L_{offset} between 0 and 1 μm for the optimum h_{offset} obtained from the first analysis (red curve). This 3D parametric analysis confirmed that the optimum value of h_{offset} is equal to 400 nm leading to a minimum coupling loss (or maximum coupling efficiency) of -1.91 dB matching the overlap integral analysis. Regarding tolerance to deviations of h_{offset} , the insertion loss increases only by 0.5 dB when h_{offset} varies $\pm 200 \text{ nm}$ from the optimal value (400 nm) and remains below 1 dB for h_{offset} variation between -270 nm and $+400 \text{ nm}$ from the optimal value (400 nm). As far as the longitudinal offset (L_{offset}) is

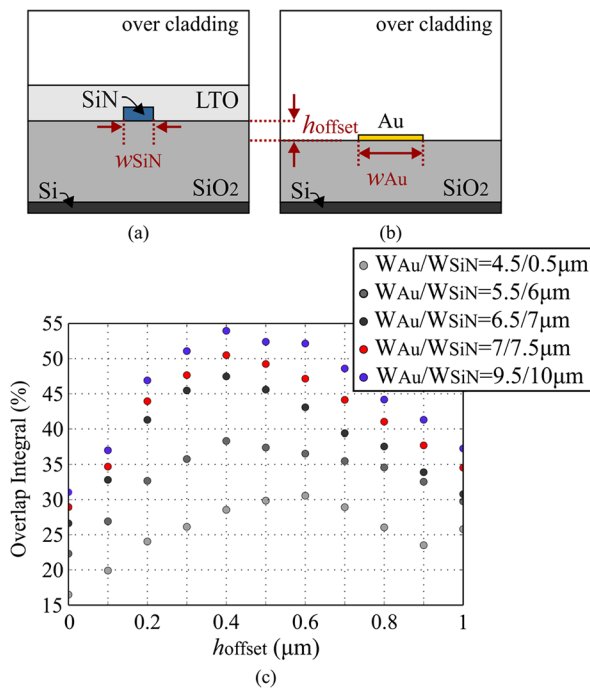
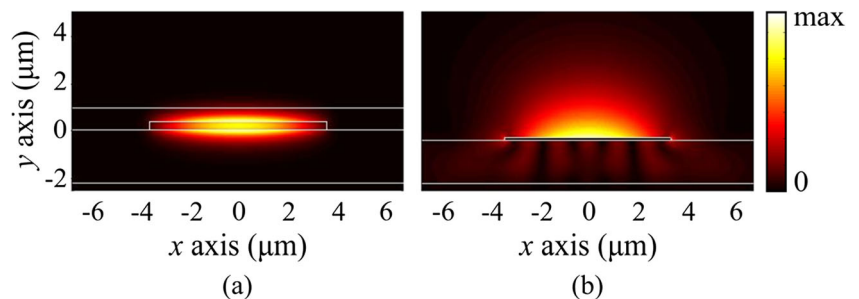


Fig. 3 **a, b** Relative position of the 2D cross-sectional geometries for the Si₃N₄ photonic and the thin-film plasmonic waveguide. **c** Overlap integral values versus vertical offset (h_{offset}) calculated for several waveguide width combinations

concerned, the 3D FDTD simulation study proved that a small increase of coupling loss is observed when L_{offset} increases. Specifically, only 0.28 dB of excessive loss is observed when L_{offset} increases from 0 to 500 nm revealing an increased tolerance of the proposed plasmophotonic interface to structural deviations of few hundreds of nanometers. Moreover, we note that even in the extreme case where L_{offset} reaches its extreme value of 1 μm extra loss remains below 1 dB.

In all the above cases, coupling losses were calculated by launching the quasi-TM mode of the 7.5- μm -wide photonic waveguide as excitation and measuring the power that has been coupled to the TM plasmonic mode at a distance of 1.5 μm away from the front-end of the Au stripe. To ensure that the calculated power transmission refers only to the TM plasmonic mode and not any power coupled to potentially excited radiation modes, the coupling loss was calculated with the aid of a built-in mode expansion technique offered by the FDTD-based simulator [36].

Fig. 4 Electric field distribution of the **a** TM photonic mode of interest and **b** the TM plasmonic thin-film mode. The dimensions utilized for the two structures have been derived from the overlap integral analysis



To investigate the broadband behavior of the thin-film configuration an additional study has been performed. Specifically, the 3D interface model has been electromagnetically simulated through FDTD analysis in a wavelength region between 1500 and 1600 nm. Figure 6 shows the coupling loss and the L_{SPP} variation within this range. Interestingly, coupling loss is slightly affected by this wavelength sweep (0.2 dB to 0.4 dB absolute deviation from the coupling loss calculated at 1550 nm) revealing a 1-dB bandwidth greater than 100 nm whereas an absolute deviation of 4 μm to 14 μm from $L_{\text{SPP}} = 86 \mu\text{m}$ at 1550 nm is observed.

This design analysis has been also experimentally verified in [16] showing the practicability of our design process. Specifically, for a fabricated structure with L_{offset} equal to 575 nm for the left (photonic-to-plasmonic) and 850 nm for the right (plasmonic-to-photonic) side of the plasmophotonic structure, an insertion loss of -2.3 ± 0.3 dB per single interface was measured which is in agreement with the expected theoretical ones for the above L_{offset} values (see red curve in Fig. 5c, -2.3 dB and -2.6 dB for $L_{\text{offset}} = 575$ nm and 850 nm, respectively).

Hybrid Slot Structure

The second coupling scheme investigated in this work adopts a hybrid plasmonic slot structure extending the structure reported in [3]. Specifically, in the cited study the whole structure is embedded in silica excluding any aqueous applications of such a hybrid configuration. In this work, we examine an open-cladded hybrid slot waveguide and we optimize coupling efficiency in a water filled slot. Moreover, we deploy Si₃N₄ for the photonic waveguide platform instead of silicon. As such, the proposed hybrid structure consists of the previously described Si₃N₄ ridge waveguide (photonic part) and an Au-based plasmonic slot element (plasmonic part) located on top of the LTO cladding of the photonic waveguide. The LTO cladding acts as a spacer between the two parts of the hybrid composite. The hybrid structure resides on a silica (SiO₂) substrate and is surrounded by a water layer to optimally mimic a potential biosensing environment. The cross-sectional geometry of this waveguide is depicted in Fig. 7a. Due to its hybrid nature, this structure is capable of supporting modes with field

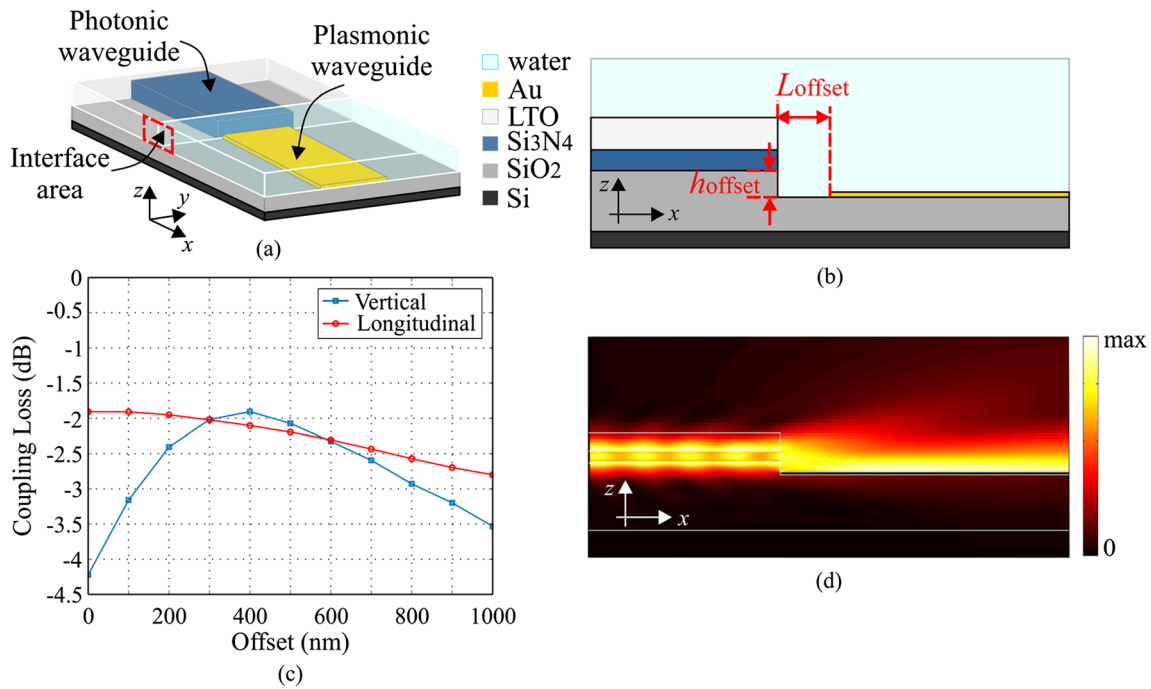


Fig. 5 **a** 3D geometry model of the photonic-to-plasmonic interface under investigation. **b** 2D side-view geometry model of the photonic-to-plasmonic interface. **c** Coupling loss versus h_{offset} for a fixed $L_{\text{offset}} =$

0 μm (blue) and versus L_{offset} (red) for the optimum h_{offset} (400 nm). **d** Electric field distribution for the optimal case

distributions in both the photonic and plasmonic part. In order to transfer light vertically from the photonic to the plasmonic part and/or backwards, the directional coupling mechanism was exploited [37, 38]. More specifically, this hybrid structure, if properly designed, can support modes that exhibit quasi-even or odd symmetry allowing for power exchange between the two branches. This power exchange can be considered as the result of the beating between the two supported modes of different symmetry. Our design analysis aims at maximizing this power transfer between the two branches by optimizing the geometry of the hybrid structure. For this

purpose, a two-step design approach has been followed. Firstly, the 2D eigenvalue problem of the structure was solved in order to detect the two hybrid modes and secondly, the power exchange mechanism was verified through a 3D FDTD simulation at 1550 nm.

Beginning with the 2D modal analysis of the hybrid slot waveguide, all the possible geometrical combinations were taken into account so that the hybrid modes can be supported. Three main geometrical parameters have been investigated: the widths of the Si₃N₄ core (w_{SiN}) and the plasmonic slot (w_{slot}) as well as the thickness of the oxide cladding layer (h_{cladding}). The height of the Si₃N₄ core has been retained equal to that of the basic Si₃N₄ ridge waveguide described in the beginning of this section, i.e., 360 nm. The thickness of the metal layer was set to 100 nm like the case of the end-fire configuration.

A finite-difference-based eigenmode solver has been also employed for the solution of this eigenmode problem [35]. Figure 7d–f summarize the results of a thorough parametrical analysis regarding the three parameters under investigation. Particularly, Fig. 7d, e contain the variation of the real part of the effective indices for the quasi-even and quasi-odd modes with respect to h_{cladding} and w_{SiN} for several values of the slot width, w_{slot} (150, 200, 250, and 300 nm), whereas the propagation length, L_{SPP} , of the pure plasmonic mode supported by the slot waveguide (without the Si₃N₄ waveguide underneath) as a function of w_{slot} is depicted in Fig. 7f. The design target is to ensure efficient light transfer between the

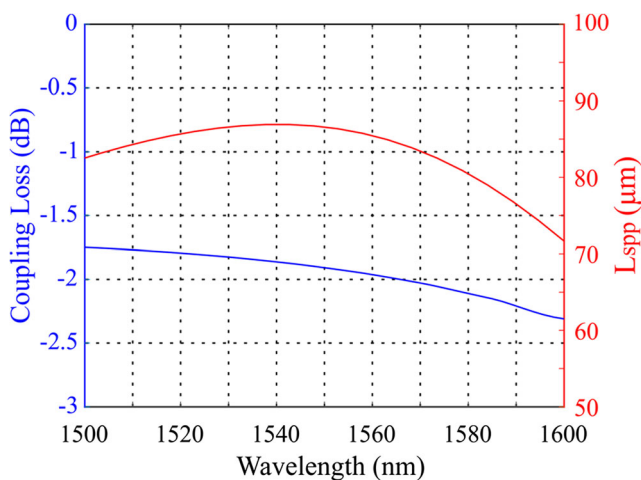


Fig. 6 Coupling loss (blue curve) and plasmonic propagation length (red curve) versus wavelength for the thin-film interface configuration

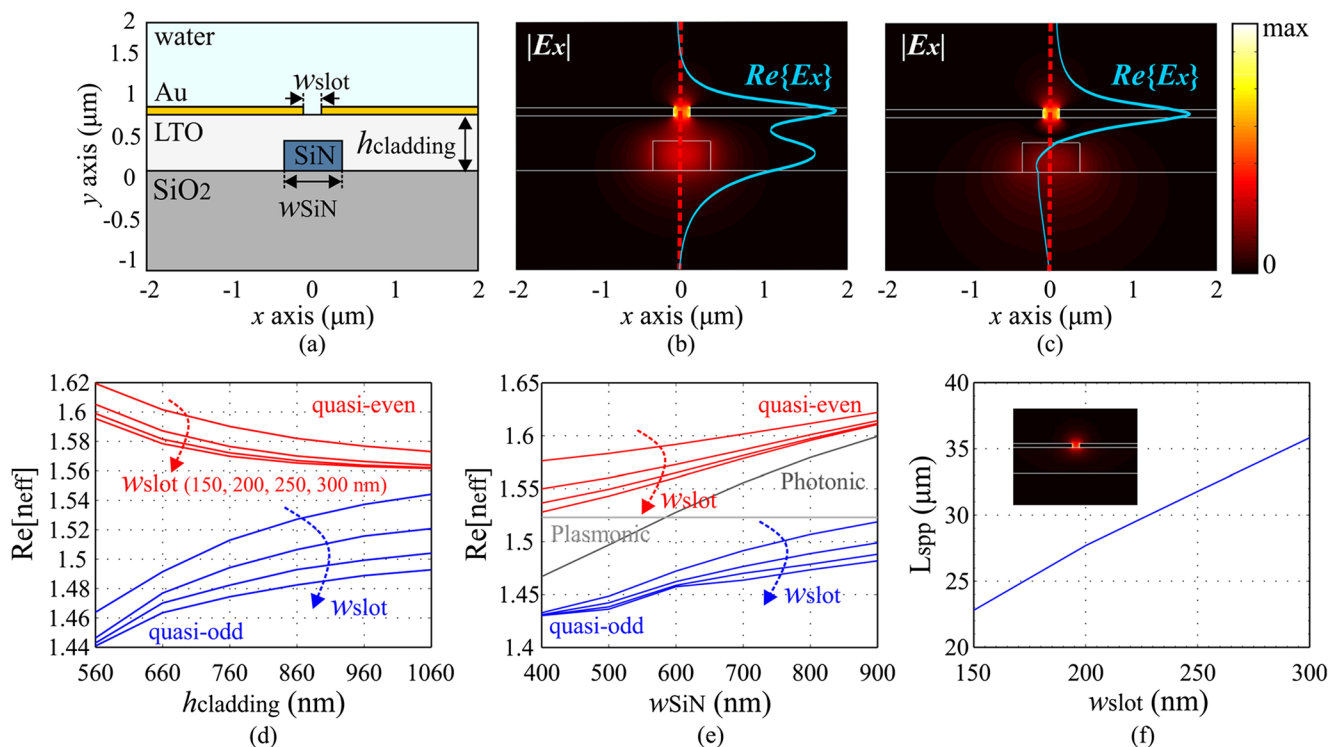


Fig. 7 **a** Cross-sectional geometry of the hybrid plasmonic waveguide structure. **b, c** Distribution of electric field dominant components (E_x) and the corresponding electric field profiles [$Re\{E_x\}$] along $x = 0$ for the two hybrid modes of interest at 1550 nm. Geometrical properties: $w_{SiN} = 700$ nm, $w_{slot} = 200$ nm, and $h_{cladding} = 660$ nm. Note the quasi-even and odd symmetry of each mode. **d** Effective index values of the two antisymmetric modes (red and blue curves) versus LTO cladding thickness

and for various metallic slot widths. The direction of the arrows indicates increasing slot widths (150, 200, 250, and 300 nm). **e** Effective index values of the two antisymmetric modes (red and blue curves) versus Si_3N_4 width and for various metallic slot values (150, 200, 250, and 300 nm). **f** Propagation length of the pure plasmonic mode (inset) versus metallic slot width

two parts within a minimum coupling length (L_c) and achieving a maximum propagation length (L_{SPP}) for the pure plasmonic section. Based on this rationale, the optimal geometry setup has been selected as follows: $w_{SiN} = 700$ nm, $w_{slot} = 200$ nm and $h_{cladding} = 660$ nm. Figure 7b, c illustrates the electric field amplitude distributions ($|E_x|$) for the two eigenmodes (quasi-even and quasi-odd) and the corresponding

electric field profiles [$Re\{E_x\}$] along $x = 0$ for the selected dimensions revealing their antisymmetric nature. The associated effective refractive indices obtained at 1550 nm are $n_{even} = 1.5842 - 0.00199i$ and $n_{odd} = 1.4751 - 0.00194i$ for the quasi-even and odd modes, respectively. The corresponding coupling length (L_c) has been calculated equal to 7 μm according to the following equation

Fig. 8 **a** 3D geometry model utilized for the 3D FDTD analysis, **b** side-view of the waveguide 3D geometry model, and **c** electric field distribution calculated on a plane in the middle of the metallic slot

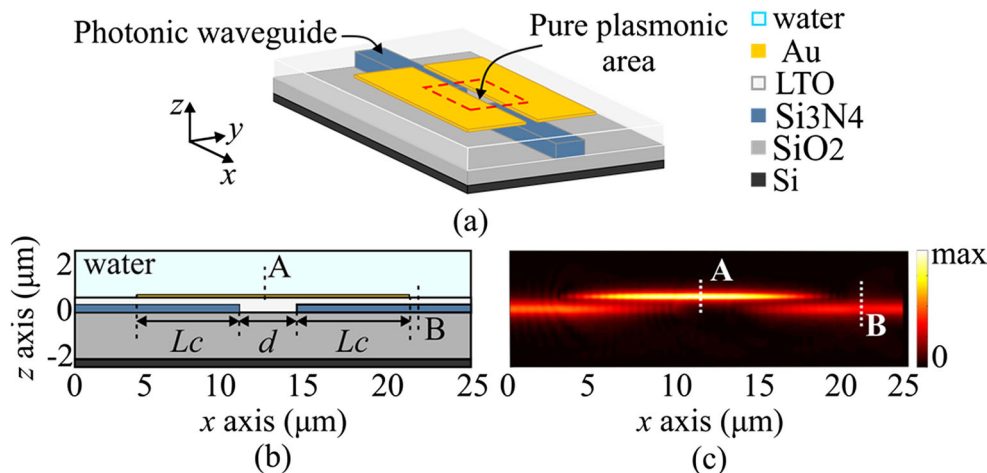


Table 1 Coupling loss for each light transition of the hybrid slot-based waveguide structure

Calculation plane	Coupling loss (dB)
A	−1.07
B	−2.31

$$L_c = \frac{\pi}{\beta_{\text{even}} - \beta_{\text{odd}}}, \quad (2)$$

where the real parts of the effective indices for each mode play an important role for its minimization [4]. The propagation length for the pure plasmonic mode has been calculated at 28 μm .

At a second phase, the hybrid slot structure was used to couple light efficiently from the pure photonic (input waveguide) to the pure plasmonic part and backwards as shown in Fig. 8a. Specifically, when the Si_3N_4 ridge is excited with the quasi-TE photonic mode (see Fig. 1b), a set of antisymmetric hybrid modes as those investigated previously is expected to be excited in the area where the two parts (plasmonic and photonic) coexist enabling the power exchange between the two branches. To further enhance this coupling mechanism, the photonic waveguide has been interrupted after a length of L_c (see Fig. 8b). This interruption aims at maintaining the coupled optical power entirely in the plasmonic slot waveguide and preventing any power from leaking to the photonic part. After a distance d of the pure plasmonic part, which was set to 4 μm for computational simplicity, a similar Si_3N_4 ridge waveguide was included in order to couple the light back to the photonic plane.

The 3D model of the above configuration has been numerically simulated using the FDTD-based solver. According to simulation results, this hybrid structure can efficiently transfer the light from the photonic to the plasmonic branch and/or backwards with efficiencies over 78% per transition corresponding to coupling losses of only −1.07 dB at the wavelength of interest (1550 nm). Figure 8b depicts a side-view of the analyzed geometry model whereas Fig. 8c shows the

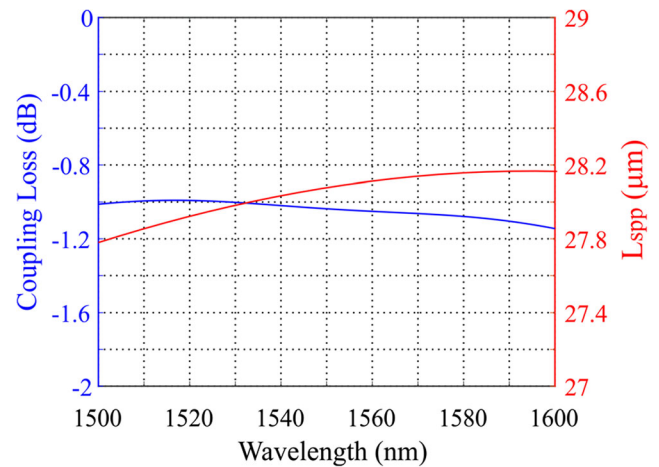


Fig. 10 Coupling loss (blue curve) and plasmonic propagation length (red curve) versus wavelength for the hybrid slot configuration

electric field distribution illustrating the light transfer. Table 1 summarizes the coupling losses calculated on the two different planes A and B (shown in Fig. 8c) representing light transition from the photonic to the plasmonic plane (A) and back to the photonic plane (B).

A device that exploits the vertical directional coupling mechanism is quite sensitive to structural deviations during fabrication. Taking this into account, we have examined the loss tolerance of the proposed plasmo-photonic configuration with respect to deviations of two critical structural parameters, that is the thickness of the LTO cladding and the possible misalignment along the x direction between the plasmonic slot and the photonic waveguide denoted as Δx in Fig. 9a. Figure 9b depicts the coupling loss with respect to h_{cladding} variations from optimal value (660 nm) calculated by means of 3D-FDTD simulations for $\Delta x = 0$ nm. The remaining geometrical parameters were kept equal to their optimal values and the interruption of the photonic waveguide retained to the initially calculated L_c value (7 μm). As can be seen in Fig. 9b, the proposed configuration is more tolerant for thicker claddings. Specifically, for a cladding thicker by

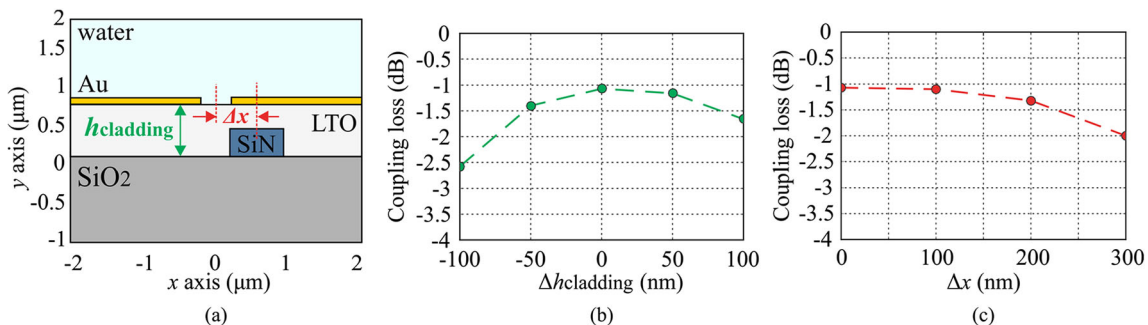
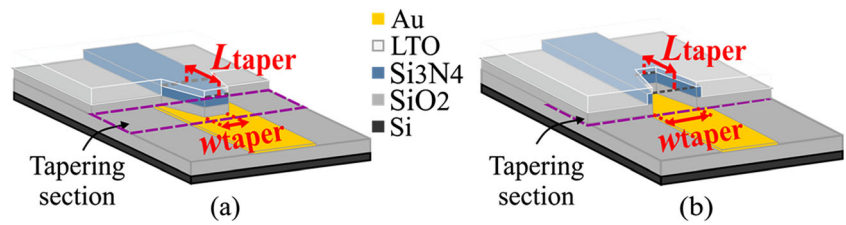


Fig. 9 a Coupling loss tolerance of the a Au-based hybrid slot structure to b variations of the LTO thickness and c misalignment of the two waveguides along x direction (Δx)

Fig. 11 3D geometries for the investigated plasmonic tapering scenarios. **a** Scenario 1 and **b** scenario 2



100 nm from its optimal value, an extra coupling loss of only 0.6 dB is introduced while for a 100 nm shorter cladding, excessive loss is about 1.5 dB. However, additional loss remains below 0.5 dB for a deviation of ± 50 nm rendering the structure quite tolerant to potential variations of the cladding’s thickness. The insertion loss as a function of longitudinal misalignment is shown in Fig. 9c where we observe that coupling loss increases gradually with an increasing Δx . Interestingly, coupling loss is minimally affected when $\Delta x = 100$ nm (0.03 dB of extra loss) while even at $\Delta x = 300$ nm excess loss remains below 1 dB. Similar results were obtained for a misalignment to the opposite direction. Thus, the configuration under investigation exhibits an increased tolerance to misalignment issues facilitating fabrication process. Once again, optimal values have been used for the remaining parameters and coupling loss was calculated by means of 3D-FDTD simulations.

The broadband behavior of the hybrid slot-based structure was also investigated. Figure 10 depicts the results in the wavelength range of 1500–1600 nm. As can be seen, for a wavelength range of 100 nm, changes below 1 dB were observed with regard to coupling loss revealing a 1-dB bandwidth greater than 100 nm whereas plasmonic propagation length was minimally affected.

Experimental characterization of such a hybrid structure can be found in [22]. Specifically, coupling loss of -2.24 ± 0.3 dB is reported for a hybrid slot configuration consisting of a 150 nm thick Au-based plasmonic slot waveguide and a $360 \text{ nm} \times 800 \text{ nm}$ Si₃N₄ photonic waveguide. Apart from the slightly different dimensions of the two waveguides, the coupling loss deviation of 1.17 dB compared to the expected value from the above numerical analysis (-1.07 dB) is also attributed to the existence of a thin Ti layer under the Au layer which contributes to extra losses.

Coupling Efficiency Optimization

An additional design step was investigated as the means to further improve coupling efficiency to the two aforementioned plasmonic waveguides. This step includes the implementation of plasmonic tapering configurations so as to achieve smoother light transitions, and thus reduced coupling losses between the photonic and the plasmonic waveguides.

End-Fire Thin-Film Structure

Regarding the end-fire thin-film structure, two tapering scenarios have been studied which are depicted in Fig. 11a, b. In both cases the inclusion of the plasmonic tapering section aims at achieving better mode matching between the injected TM photonic mode and the plasmonic one eliminating modal reflection at the interface and, thus, increasing coupling efficiency. For this purpose, two main parameters were investigated for each scenario, i.e., the width (w_{taper}) and the length of the taper (L_{taper}) (see Fig. 11), whereas the rest of the geometry has been retained identical to the optimal design presented in the previous section to allow for comparison.

After a detailed 3D FDTD parametrical study, the simulation results revealed marginal improvement of coupling efficiency in the order of 0.07–0.12 dB compared to the initial scenario without the plasmonic tapering scheme. The minimal improvement is attributed to the fact that in both tapering scenarios although the transition is smoother, a discontinuity and mode mismatch between the two waveguides still exist. The exact coupling loss values along with the optimal tapering geometry for each scenario are listed in Table 2. For comparison reasons, the coupling loss value for the initial case (without the plasmonic taper) has been also included in this table.

Table 2 Comparative coupling loss values for the various thin-film plasmonic tapering scenarios

	Coupling loss (dB)	Optimal tapering geometry
Tapering scenario 1	-1.84	$L_{taper} = 0.5 \text{ } \mu\text{m}$ $w_{taper} = 6.5 \text{ } \mu\text{m}$
Tapering scenario 2	-1.79	$L_{taper} = 0.5 \text{ } \mu\text{m}$ $w_{taper} = 4.5 \text{ } \mu\text{m}$
Without taper	-1.91	

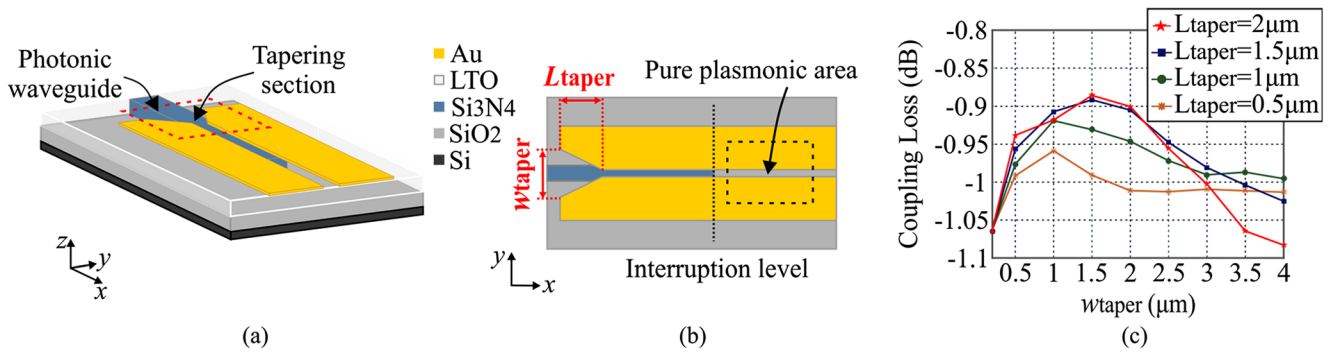


Fig. 12 Plasmonic tapering scheme for the hybrid slot configuration **a** 3D geometry model for the proposed tapering scenario. **b** 2D top-view of the proposed tapering scenario. **c** Coupling loss versus w_{taper} for several L_{taper} values

Hybrid Slot Structure

In the same rationale, a plasmonic tapering method in the hybrid slot structure described previously has been also investigated. Coupling efficiency improvement has been pursued by introducing a plasmonic taper section that serves as an intermediate mode transducer between the pure photonic waveguide and the final targeted hybrid slot structure. The 3D geometry as well as a 2D top-view of the proposed configuration can be seen in Fig. 12a, b. As in the case of the thin-film configuration, the tapering section is expected to limit the reflected power from the photonic-to-plasmonic interface rendering the light transition smoother and, thus, the coupling mechanism more efficient. Towards this direction, the 3D geometry model of the proposed structure has been parametrically investigated through 3D FDTD simulations.

The two main parameters which have been investigated are the width (w_{taper}) and the length of the taper section (L_{taper}) (Fig. 12b). Figure 12c shows the obtained results from this parametrical study. More specifically, the variation of coupling loss with respect to w_{taper} seems to exhibit a local minimum (considering its absolute value) for $w_{\text{taper}} = 1.5 \mu\text{m}$. As the length of the taper (L_{taper}) takes larger values this local minimum decreases till the value of $L_{\text{taper}} = 1.5 \mu\text{m}$ beyond which any increase of L_{taper} does not offer significant improvement. Therefore, the optimal choice for this configuration includes $w_{\text{taper}} = 1.5 \mu\text{m}$ and $L_{\text{taper}} = 1.5 \mu\text{m}$ leading to a

coupling loss value in the sub-dB region of 0.89 dB, providing a clear added value of the proposed tapering scheme.

Design with CMOS Metals

Having completed the design analysis and efficiency optimization of both plasmo-photonic coupling schemes with gold as the plasmonic metal material, we then proceeded to the deployment of CMOS-compatible metals by replacing Au with aluminum and copper. In this section, the influence of the CMOS metals in both optimized plasmo-photonic waveguides is evaluated.

End-Fire Thin-Film Structure

As in the case of the Au-based, end-fire thin-film configuration, the design study for the CMOS-based thin-film structure begins with a 2D eigenvalue analysis on the cross-sections of the waveguides under investigation. The coupling mechanism for this end-fire structure is expected to be governed by the same principles as the case of Au, so spatial mode matching should be achieved in order to efficiently transfer the light from the photonic to the plasmonic waveguide. The power overlap integral analysis described in the previous section has been repeated leading to similar results for the dimensions of the two

Fig. 13 Electric field distribution for the TM plasmonic mode of interest for **a** the Al-based waveguide and **b** the Cu-based waveguide

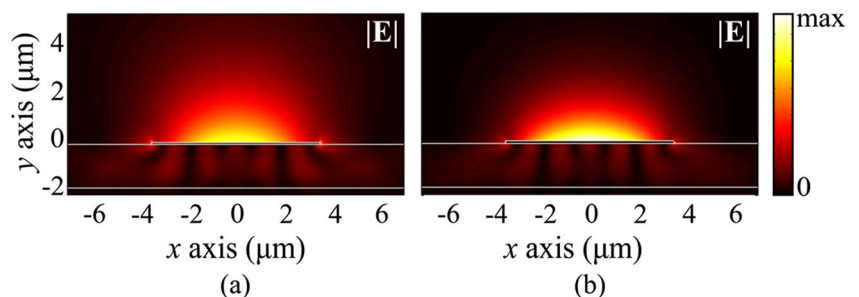
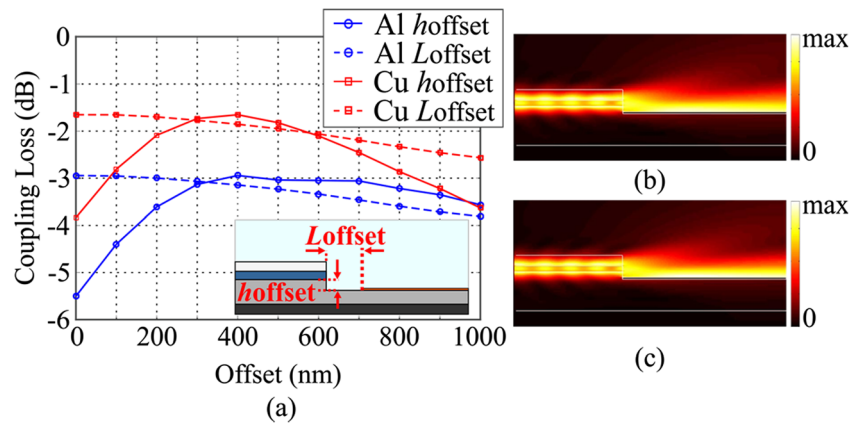


Fig. 14 **a** Coupling loss versus h_{offset} for a fixed $L_{\text{offset}} = 0 \mu\text{m}$ and versus L_{offset} for the optimum h_{offset} for both CMOS metals. **b, c** Electric field distribution along the light propagation direction for optimal ($L_{\text{offset}} = 0 \text{ nm}$, $h_{\text{offset}} = 400 \text{ nm}$) Al-based structure and Cu-based structure, respectively



waveguide structures under study (Si_3N_4 photonic and thin-film plasmonic waveguide) both for Al-based ($n_{\text{Al}} = 1.42\text{--}15.1i$ [31]) and Cu-based ($n_{\text{Cu}} = 0.26\text{--}9.8i$ [31]) plasmonic structures.

To have a fair comparison between the different metal materials the same dimensions of the Si_3N_4 photonic and Au-based thin-film plasmonic waveguides have been retained, i.e., $360 \text{ nm} \times 7.5 \mu\text{m}$ for the Si_3N_4 photonic core and $100 \text{ nm} \times 7 \mu\text{m}$ for the metallic thin-film stripe. It is shown that, for these dimensions at the wavelength of interest (1550 nm), the fundamental TM plasmonic mode is supported by both the Al- and the Cu-based thin-film waveguides (Fig. 13a, b) having an electric field distribution similar to the one of the Au-based structure (Fig. 4b). The effective indices derived from this 2D eigenmode study were $n_{\text{eff}}^{\text{Al}} = 1.312\text{--}0.00196i$ and $n_{\text{eff}}^{\text{Cu}} = 1.319\text{--}0.00156i$ corresponding to propagation lengths (L_{SPP}) of $63 \mu\text{m}$ and $79 \mu\text{m}$ for the Al- and the Cu-based structure, respectively.

An end-fire interface configuration similar to the one depicted in Fig. 5a has been analyzed by means of 3D FDTD numerical simulations adopting Al and Cu as the plasmonic metal material. The effect of both vertical (h_{offset}) and longitudinal (L_{offset}) offset distances on induced coupling loss of the plasmophotonic interface has been investigated. Figure 14a shows the results of this numerical analysis for both Al and Cu. As it can be seen, for both the Al- and the Cu-based structure the variation of coupling loss with respect to h_{offset} exhibits a local minimum (regarding absolute value) at $h_{\text{offset}} = 400 \text{ nm}$ corresponding to stronger coupling. At the same time, the variation of coupling loss versus L_{offset} exhibits a monotonically decreasing behavior signifying that the minimum achieved coupling loss is obtained for $L_{\text{offset}} = 0 \text{ nm}$ for both CMOS metal materials and increases gradually with increasing L_{offset} . Moreover, the end-fire structure based on Cu seems to have better performance in terms of coupling efficiency when compared to Al. As such, the minimum achieved coupling loss for $L_{\text{offset}} = 0 \text{ nm}$ and $h_{\text{offset}} = 400 \text{ nm}$ has been calculated at -2.94 dB and -1.65 dB for

Al and Cu, respectively. Figure 14b, c illustrate the electric field distributions along the light propagation direction for both CMOS metals.

Regarding tolerance to structural deviations, the insertion loss remains below 1 dB when h_{offset} varies between -250 and $+600 \text{ nm}$ from the optimal value (400 nm) for the Al-based structure and between -280 and $+370 \text{ nm}$ from the optimal value (400 nm) for the Cu-based structure. Additionally, only 0.3 dB of excessive loss is observed when L_{offset} increases from 0 to 500 nm for both CMOS metals and remains below 1 dB even when L_{offset} reaches the extreme value of $1 \mu\text{m}$ suggesting again high tolerance of the proposed plasmophotonic interface to fabrication inaccuracies of few hundreds of nanometers.

The broadband functionality of the CMOS end-fire structures was also investigated in the wavelength region 1500 nm–1600 nm. As illustrated in Fig. 15, small deviations in coupling loss and in plasmonic propagation length (L_{SPP}) are observed for both metals when the wavelength deviates from 1500 to 1600 nm rendering the CMOS end-fire configurations functionally tolerant in this wavelength range

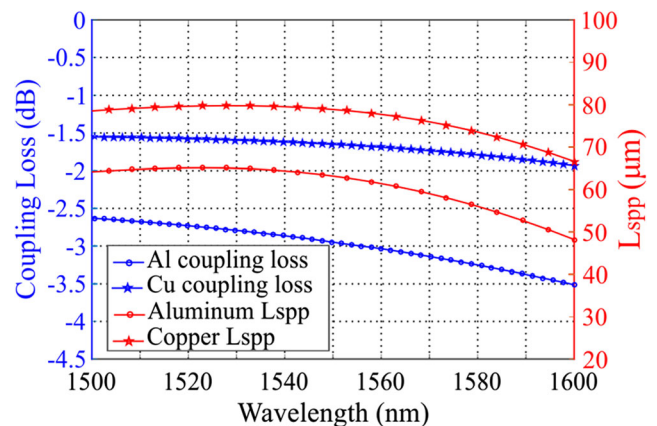


Fig. 15 Coupling loss (blue curves) and plasmonic propagation length (red curves) versus wavelength for the end-fire CMOS configurations

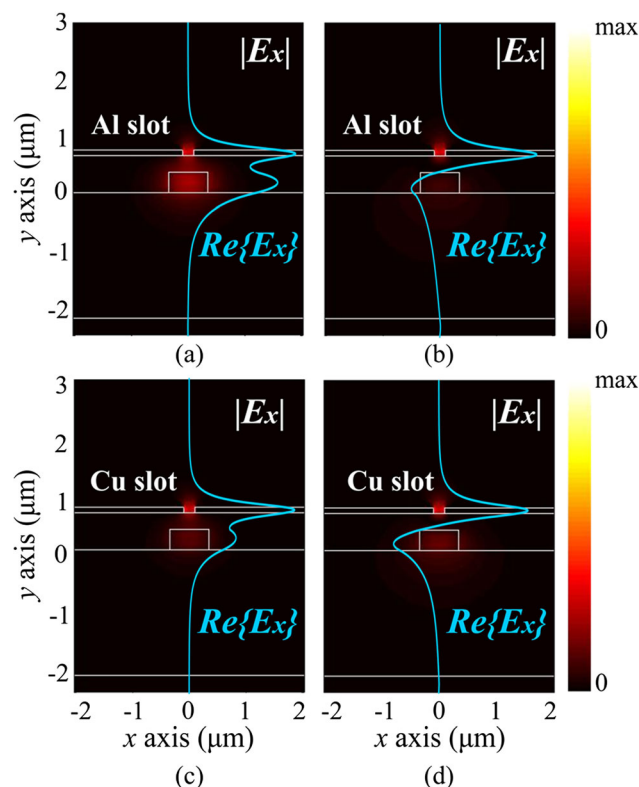


Fig. 16 Distribution of electric field dominant components ($|E_x|$) for the two hybrid modes at 1550 nm. Note the quasi-even and odd symmetry of each mode. **a** Quasi-even mode of Al-based hybrid structure. **b** Quasi-odd mode of Al-based hybrid structure. **c** Quasi-even mode of Cu-based hybrid structure, and **d** quasi-odd mode of Cu-based hybrid structure

indicating again a 1-dB bandwidth greater than 100 nm regarding coupling loss.

Furthermore, the addition of plasmonic tapers was also investigated yet no improvement was observed for the Al-based structure while only marginal benefits were detected for the Cu-based similarly to gold (0.034 dB improvement in coupling efficiency for the first tapering scenario and 0.09 dB improvement for the second tapering scenario).

Hybrid Slot Structure

The same CMOS materials were investigated in the off-plane directional coupling scheme based on the hybrid slot structure described in the first section. Relying on this structure (Fig. 7a), the Au metallic layers are replaced with Al and Cu and the whole configuration is simulated so that optimal geometry dimensions are obtained. As already explained, if properly designed, the structure is capable of supporting hybrid modes of different symmetry (quasi-even and quasi-odd) which have field distributions in both their photonic and plasmonic part. Thus, the power transfer between these two branches can result from the beating of the two antisymmetric modes.

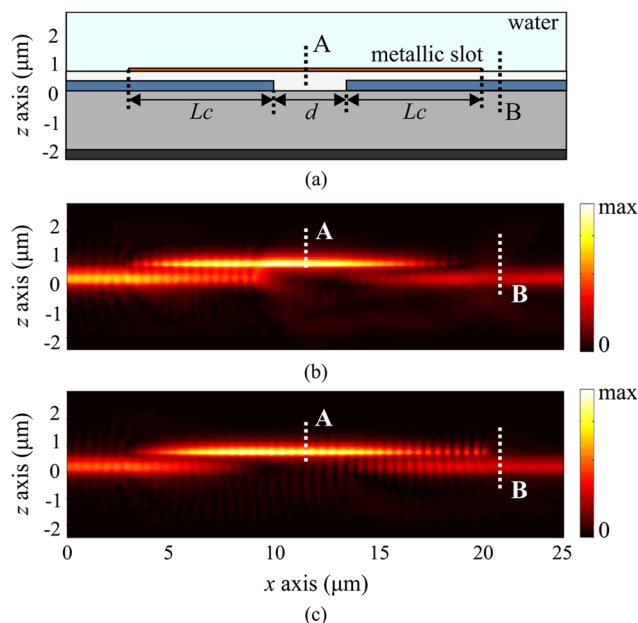


Fig. 17 **a** Side-view of the hybrid waveguide model under study. **b, c** Electric field distributions calculated on a plane in the middle of the metallic slot for Al- and Cu-based configurations, respectively

To detect these hybrid modes and determine the optimal cross-sectional dimensions, we begin with the 2D eigenmode analysis of the hybrid structure. For this purpose, a thorough investigation of all the possible combinations of the three main geometrical parameters (w_{SiN_4} , w_{slot} , and h_{cladding} with respect to Fig. 7a) has been performed for both Al and Cu. Once again, the height of the Si_3N_4 core and the thickness of the metal layer have been retained to 360 nm and 100 nm, respectively. The above parametric analysis revealed that the structures with the CMOS metallic layers behave in a similar manner as the Au-based structure. As such, the selected optimal geometry has been the same with the one selected for the Au-based hybrid structure, i.e., $w_{\text{SiN}_4} = 700$ nm, $w_{\text{slot}} = 200$ nm, and $h_{\text{cladding}} = 660$ nm. For these dimensions, the electric field distributions ($|E_x|$) for the two eigenmodes (quasi-even and quasi-odd) and the associated electric field profiles [$\text{Re}(E_x)$] along $x = 0$ are depicted in Fig. 16a–d for both Al and Cu. The corresponding effective refractive indices obtained at 1550 nm for the Al-based structure were calculated $n_{\text{even}}^{\text{Al}} = 1.562 - 0.003219i$ and $n_{\text{odd}}^{\text{Al}} = 1.443 - 0.004963i$ whereas the equivalent ones for the Cu-based configuration were $n_{\text{even}}^{\text{Cu}} = 1.592 - 0.003323i$ and $n_{\text{odd}}^{\text{Cu}} = 1.48 - 0.002456i$. These values lead to a coupling length equal to 6.5 μm for the case of Al and 7 μm for the case

Table 3 Coupling loss along the CMOS hybrid slot structure

Metal	Plane A	Plane B
Al	−2.31 dB	−6.48 dB
Cu	−1.38 dB	−3.52 dB

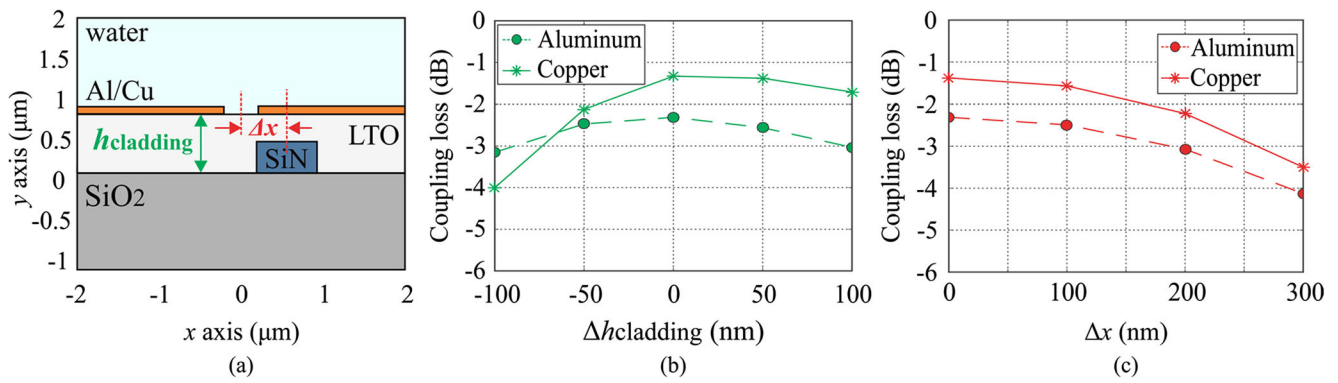


Fig. 18 Coupling loss tolerance of the **a** CMOS-based hybrid slot structure to **b** variations of the LTO thickness and **c** misalignment of the two waveguides along *x* direction (Δx)

of Cu according to (2). Regarding the pure plasmonic waveguide branch, the propagation length has been estimated at 12 μm and 21 μm for Al and Cu, respectively.

The 3D models of the above CMOS hybrid configurations have been analyzed next by means of 3D FDTD numerical simulations. Figure 17a illustrates a side view of this 3D geometry model also showing the interruption of the photonic branch after a length equal to L_c . The pure plasmonic area is defined by the distance d , which has been retained at 4 μm for comparison reasons. Figure 17b, c depicts the electric field distributions calculated on a plane in the middle of the metallic slot when Al and Cu are utilized as the plasmonic metal materials, respectively; whereas Table 3 summarizes the total coupling losses calculated on two different planes A and B representing light transition from the photonic to the plasmonic plane (A) and back to the photonic plane (B).

Tolerance of the CMOS-based configuration to variations of the LTO thickness and the longitudinal misalignment between the photonic and plasmonic waveguide was also examined. The obtained results are depicted in Fig. 18b, c. Regarding the Al-based structure, coupling loss is minimally affected for a cladding thickness deviation of ± 50 nm (0.16 dB–0.25 dB) whereas for a deviation of ± 100 nm excessive loss remains below 1 dB (0.72 dB–0.84 dB). As far as the longitudinal misalignment is concerned, only 0.18 dB and 0.76 dB of excessive loss is observed for 100 nm and 200 nm of misalignment, respectively, indicating again a high-tolerant configuration. Regarding the Cu-based structure, simulation results revealed high tolerance to positive LTO cladding variations (thicker than optimum). However, extra coupling loss is below 1 dB for a cladding shorter than the designed by 50 nm as well. Additionally, only 0.19 dB of extra loss is observed for 100 nm of misalignment and remains below 1 dB when 200 nm of misalignment is introduced indicating again a high-tolerant configuration.

The CMOS-based hybrid slot configurations were also investigated in the wavelength region 1500 nm–1600 nm. Figure 19 illustrates the results of this investigation which reveal that for a 100 nm wavelength range L_{SPP} is almost stable and changes below 1 dB are observed regarding coupling loss revealing a 1-dB bandwidth greater than 100 nm.

In the last step, further optimization via the implementation of a plasmonic taper was also examined taking into account the remarkable improvement of coupling efficiency in the case of Au. The geometry of the proposed taper is the same as the one utilized for the corresponding Au-based hybrid structure depicted in Fig. 12a, b. Parametric analysis, showed that the coupling loss per single transition was further reduced to -2.07 dB for the Al-based hybrid structure and -1.15 dB for the Cu-based structure confirming the benefits provided by the tapering approach in the slot waveguide configuration. The optimal taper dimensions that led to those values were $L_{\text{taper}} = 2$ μm and $w_{\text{taper}} = 4$ μm for the case of Al and $L_{\text{taper}} = 2$ μm and $w_{\text{taper}} = 1.5$ μm for the case of Cu.

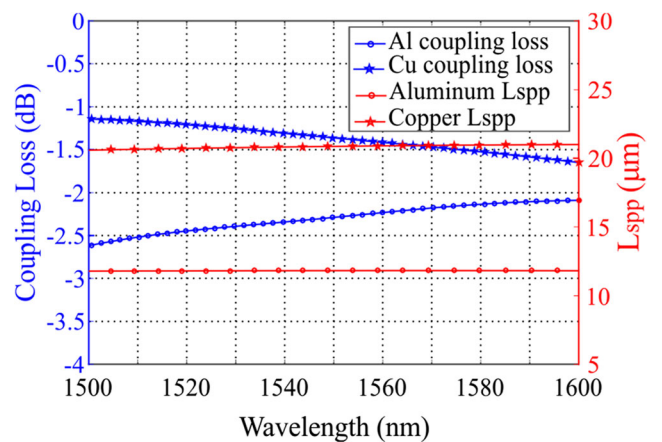


Fig. 19 Coupling loss (blue curves) and plasmonic propagation length (red curves) versus wavelength for the two CMOS hybrid slot configurations

Table 4 Overview of the investigated coupling schemes

End-fire thin-film structure						Directional coupling hybrid structure						
Losses ^a (dB)	A_{eff} (μm^2)	L_{spp} (μm)	Tolerance—excessive loss < 1 dB			Losses ^a (dB)	A_{eff} (μm^2)	L_{spp} (μm)	Tolerance—Excessive loss < 1 dB			
			h_{offset} (nm)		L_{offset} (nm)				h_{cladding} (nm)		Δx (nm)	
			LS dev. ^b	RS dev. ^c	Dev.				LS dev. ^b	RS dev. ^c	Dev.	
Au	− 1.79	10.88	86	− 270	+ 400	1000	− 0.89	0.124	28	− 80	+ 100	± 300
Al	− 2.94	17.63	63	− 250	+ 600	1000	− 2.07	0.158	12	− 50	+ 100	± 200
Cu	− 1.56	9.37	79	− 280	+ 370	1000	− 1.15	0.126	21	− 100	+ 100	± 200

^a With plasmonic taper

^b Left side (LS) deviation from optimal value

^c Right side (RS) deviation from optimal value

Overview and Discussion

In order to compare the investigated coupling schemes and their performance for the different metals, the main results derived in this work are summarized in Table 4. Apart from coupling loss and propagation length, the effective mode area (A_{eff}) was also calculated for each case according to the following equation

$$A_{\text{eff}} = \frac{\left(\iint |\mathbf{E}_{pl}|^2 dA \right)^2}{\iint |\mathbf{E}_{pl}|^4 dA}, \tag{3}$$

where \mathbf{E}_{pl} describes the vector of the electric field distribution of the plasmonic mode of interest and A is the area over which the surface integral and \mathbf{E}_{pl} are numerically calculated [39]. Fabrication tolerances of the structures with respect to structural deviations that lead to excessive loss below 1 dB are also included in this table. The tolerance is given as deviation from the optimal value of each geometrical parameter that is 400 nm for h_{offset} , 0 nm for L_{offset} and Δx , and 660 nm for h_{cladding} .

Interestingly, CMOS-based plasmo-photonic configurations exhibit similar performance with Au-based counterparts providing evidence of the clear potential of low-cost metals to replace noble counterparts in future plasmo-photonic integrated circuits. Regarding differences between the two coupling schemes, the end-fire scenario provides longer propagation distances for the pure plasmonic parts at the expense of mode compactness (larger values of A_{eff}), whereas the directional coupling scenarios can offer nanoscale confinement of light by reducing the effective mode area two orders of magnitude but with higher propagation losses in the pure plasmonic regions by factors greater than three. Moreover, the directional coupling schemes are capable of achieving lower coupling loss reaching sub-dB values per interface when plasmonic

tapers are introduced for the case of Au and close to 1 dB values for the Cu-based CMOS-compatible configuration. Additionally, both coupling schemes are highly tolerant to deviations of key geometrical parameters as high as few hundred on nanometers both in the vertical (h_{offset} , h_{cladding}) and horizontal direction (L_{offset} , Δx), with the acceptable horizontal misalignment being even higher in the case of thin-film (L_{offset}), thus, facilitating fabrication process.

Conclusion

In summary, we have designed open-cladded plasmonic waveguides integrated on Si_3N_4 photonic platform and we have investigated methods to optimize the coupling approaches for their integration with photonic waveguides targeting CMOS manufacturing. Two approaches have been implemented (i) an in-plane end-fire interface based on a thin-film plasmonic structure and (ii) an out-of-plane directional coupling scheme based on hybrid slot module. Both coupling scenarios have been thoroughly investigated by means of electromagnetic simulations so as to efficiently transfer light from the hosting photonic platform to the plasmonic waveguides. The study was initially conducted utilizing gold as the plasmonic metal and that was subsequently extended to the CMOS-compatible metals of aluminum and copper revealing similar performance. After exhaustive investigation, we achieved high-tolerant coupling schemes with insertion losses per interface even in the sub-dB region for the Au-based hybrid slot structure and close to 1 dB values for the Cu-based CMOS-compatible configurations rendering the reported outcomes promising for CMOS-manufactured plasmonic-augmented photonic integrated circuits with superior performance and acceptable chip losses.

Acknowledgments This work is supported by the European H2020-EU.2.1.1 project PlasmFab (Contract No. 688166).

References

- Barnes WL, Dereux A, Ebbesen TW (2003) Surface plasmon sub-wavelength optics. *Nature* 424:824–830
- Gramotnev DK, Bozhevolnyi SI (2010) Plasmonics beyond the diffraction limit. *Nat Photonics* 4:83–91
- Delacour C, Blaize S, Grosse P, Fedeli JM, Bruyant A, Salas-Montiel R, Lerondel G, Chelnokov A (2010) Efficient directional coupling between silicon and copper plasmonic nanoslot waveguides: toward metal–oxide–silicon nanophotonics. *Nano Lett* 10(8):2922–2926
- Li Q, Qiu M (2010) Structurally-tolerant vertical directional coupling between metal-insulator-metal plasmonic waveguide and silicon dielectric waveguide. *Opt Express* 18(15):15531–15543
- Melikyan A, Kohl M, Sommer M, Koos C, Freude W, Leuthold J (2014) Photonic-to-plasmonic mode converter. *Opt Lett* 39(12):3488–3491
- Zhu S, Liow T, Lo G, Kwong D Fully (2011) CMOS compatible subwavelength plasmonic slot waveguides for Si electronic-photonic integrated circuits. *Optical Fiber Communication Conference/National Fiber Optic Engineers Conference. OThV5*
- Melikyan A, Alloatti L, Muslija A, Hillerkuss D, Schindler PC, Li J, Palmer R, Kom D, Muehlbrandt S, Thourhout DV, Chen B, Dinu R, Sommer M, Koos C, Kohl M, Freude W, Leuthold J (2014) High-speed plasmonic phase modulators. *Nat Photonics* 8:229–233
- Chen CT, Xu X, Hosseini A, Pan Z, Chen RT (2015) High efficiency silicon strip waveguide to plasmonic slot waveguide mode converter. *Proc SPIE* 9368:936809
- Haffner C, Heni W, Fedoryshyn Y, Niegemann J, Melikyan A, Elder DL, Baeuerle B, Salamin Y, Josten A, Koch U, Hoessbacher C, Ducry F, Juchli L, Emboras A, Hillerkuss D, Kohl M, Dalton LR, Leuthold J (2015) All-plasmonic Mach–Zehnder modulator enabling optical high-speed communication at the microscale. *Nat Photonics* 9:525–528
- Sun X, Dai D, Thylén L, Wosinski L (2015) High-sensitivity liquid refractive-index sensor based on a Mach-Zehnder interferometer with a double-slot hybrid plasmonic waveguide. *Opt Express* 23(20):25688–25699
- Nielsen MP, Lafone L, Rakovich A, Sidiropoulos T, Rahmani M, Maier SA, Oulton RF (2016) Adiabatic nanofocusing in hybrid gap plasmon waveguides on the silicon-on-insulator platform. *Nano Lett* 16(2):1410–1414
- Briggs RM, Grandidier J, Burgos SP, Feigenbaum E, Atwater HA (2010) Efficient coupling between dielectric-loaded plasmonic and silicon photonic waveguides. *Nano Lett* 10(12):4851–4857
- Papaioannou S, Vysokinos K, Tsilipakos O, Ptilakis A, Hassan K, Weeber J-C, Markey L, Dereux A, Bozhevolnyi SI, Miliou A, Kriezis E, Pleros N (2011) A 320 Gb/s-throughput capable 2x2 silicon-plasmonic router architecture for optical interconnects. *J Lightwave Technol* 29(21):3185–3195
- Tsilipakos O, Ptilakis A, Yioultsis TV, Papaioannou S, Vysokinos K, Kalavrouziotis D, Giannoulis G, Apostolopoulos D, Avramopoulos H, Tekin T, Baus M, Karl M, Hassan K, Weeber J-C, Markey L, Dereux A, Kumar A, Bozhevolnyi SI, Pleros N, Kriezis EE (2012) Interfacing dielectric-loaded plasmonic and silicon photonic waveguides: theoretical analysis and experimental demonstration. *IEEE J Quantum Electron* 48:678–687
- Papaioannou S, Kalavrouziotis D, Vysokinos K, Weeber J-C, Hassan K, Markey L, Dereux A, Kumar A, Bozhevolnyi SI, Baus M, Tekin T, Apostolopoulos D, Avramopoulos H, Pleros N (2012) Active plasmonics in WDM traffic switching applications. *Sci Rep* 2:65
- Dabos G, Ketzaki D, Manolis A, Markey L, Weeber J-C, Dereux A, Giesecke A-L, Porschatis C, Chmielak B, Tsiokos D, Pleros N (2018) Plasmonic stripes in aqueous environment co-integrated with Si₃N₄ photonics. *IEEE Photonics J* 10(1):1–8
- Dabos G, Manolis A, Papaioannou S, Tsiokos D, Markey L, Weeber J-C, Dereux A, Giesecke A-L, Porschatis C, Chmielak B, Pleros N (2018) CMOS plasmonics in WDM data transmission: 200 Gb/s (8 x 25Gb/s) transmission over aluminum plasmonic waveguides. *Opt Express* 26(10):12469–12478
- Wan R, Liu F, Tang X, Huang Y, Peng J (2009) Vertical coupling between short range surface plasmon polariton mode and dielectric waveguide mode. *Appl Phys Lett* 94(14):141104
- Liu F, Wan R, Li Y, Huang Y, Miura Y, Ohnishi D, Peng J (2009) Extremely high efficient coupling between long range surface plasmon polariton and dielectric waveguide mode. *Appl Phys Lett* 95(9):091104
- Fan B, Liu F, Li Y, Huang Y, Miura Y, Ohnishi D (2012) Refractive index sensor based on hybrid coupler with short-range surface plasmon polariton and dielectric waveguide. *Appl Phys Lett* 100(11):111108
- Zhu S, Lo G, Kwong D (2013) Silicon nitride based plasmonic components for CMOS back-end-of-line integration. *Opt Express* 21(20):23376–23390
- Dabos G, Ketzaki D, Manolis A, Chatzianagnostou E, Markey L, Weeber J-C, Dereux A, Giesecke A-L, Porschatis C, Chmielak B, Tsiokos D, Pleros N (2018) Water cladded plasmonic slot waveguide vertically coupled with Si₃N₄ photonics. *IEEE Photonics J* 10(3):1–8
- Maksymov IS, Kivshar YS (2013) Broadband light coupling to dielectric slot waveguides with tapered plasmonic nanoantennas. *Opt Lett* 38(22):4853–4856
- Baets R, Subramanian AZ, Clemmen S, Kuyken B, Bienstman P, Thomas NL, Roelkens G, Thourhout DV, Helin P, Severi S (2016) Silicon photonics: silicon nitride versus silicon-on-insulator. *Optical Fiber Communication Conference:Th3J1*
- Rahim A, Ryckeboer E, Subramanian AZ, Clemmen S, Kuyken B, Dhakal A, Raza A, Hermans A, Muneeb M, Dhoore S, Li Y, Dave U, Bienstman P, Thomas NL, Roelkens G, Thourhout DV, Helin P, Severi S, Rottenberg X, Baets R (2017) Expanding the silicon photonics portfolio with silicon nitride photonic integrated circuits. *J Lightwave Technol* 35(4):639–649
- Sacher W, Huang Y, Lo G-Q, Poon J (2015) Multilayer silicon nitride-on-silicon integrated photonic platforms and devices. *J Lightwave Technol* 33(4):901–910
- Zektzer R, Desiatov B, Mazurski N, Bozhevolnyi SI, Levy U (2014) Experimental demonstration of CMOS-compatible long-range dielectric loaded surface plasmon waveguides (LR-DLSPWs). *Opt Express* 22(18):22009–22017
- Kravets VG, Jalil R, Kim Y-J, Ansell D, Aznakayeva D, Thackray B, Britnell L, Belle B, Withers F, Radko I, Han Z, Bozhevolnyi S, Novoselov K, Geim A, Grigorenko A (2014) Graphene-protected copper and silver plasmonics. *Sci Rep* 4:5517
- Fedyanin DY, Yakubovskiy DI, Kirtaev RV, Volkov VS (2016) Ultralow-loss CMOS copper plasmonic waveguides. *Nano Lett* 16:362–366
- Lotan O, Smith C, Bar-David J, Mortensen NA, Kristensen A, Levy U (2016) Propagation of channel plasmons at the visible regime in aluminum v-groove waveguides. *ACS Photonics* 3:2150–2157

31. Weeber J-C, Arocas J, Heintz O, Markey L, Viarbitskaya S, Colas-Des-Francis G, Hammani K, Dereux A, Hoessbacher C, Koch U, Leuthold J, Rohrer K, Giesecke A-L, Porschatis C, Wahlbrink T, Chmielak B, Pleros N, Tsiokos D (2017) Characterization of CMOS metal based dielectric loaded surface plasmon waveguides at telecom wavelengths. *Opt Express* 25(1):394–408
32. Berini P (2001) Plasmon-polariton waves guided by thin lossy metal films of finite width: bound modes of asymmetric structures. *Phys Rev B* 63:125417
33. Luke K, Okawachi Y, Lamont MRE, Gaeta AL, Lipson M (2015) Broadband mid-infrared frequency comb generation in a Si_3N_4 microresonator. *Opt Lett* 40(21):4823–4826
34. Palik ED (1998) Handbook of optical constants of solids I-III. Academic Press, Orlando
35. Lumerical Solutions, Inc., <http://www.lumerical.com/tcad-products/mode/>
36. Lumerical Solutions, Inc. <http://www.lumerical.com/tcad-products/fdtd/>
37. Yariv A (1973) Coupled-mode theory for guided-wave optics. *IEEE J Quantum Electron* 9:919–933
38. Huang WP (1994) Coupled-mode theory for optical waveguides: an overview. *J Opt Soc Am A* 11:963–983
39. Agrawal GP (2007) Nonlinear Fiber optics. Academic Press